PCCP

ROYAL SOCIETY OF CHEMISTRY

PAPER

View Article Online
View Journal | View Issue

Cite this: *Phys. Chem. Chem. Phys.*, 2025, **27**, 17384

Enhancement of the triplet photosensitizing ability of BODIPY dyes by controlled red-shifted H-aggregate formation using ionic liquids: insights from spectroscopy, microscopy, DFT and biological studies

Nayana Nupur Das,[a] Soumyaditya Mula,[bc] Dhanya Rajendrababu,[d] Sivan Velmathi *[a] and Debashis Majhi *[a]

We report an innovative, straightforward, and effective supramolecular method for converting fluorophores into photosensitizers using symmetrical imidazolium ionic liquids (ILs) *via* the aggregation of BODIPY derivatives. By utilizing "red-shifted H-aggregates" of 2,6-diethyl-4,4-difluoro-1,3,5,7-tetramethyl-8-phenyl-4-bora-3a,4a-diaza-*s*-indacene (R6-BDP), along with both shorter and longer cationic alkyl chain symmetrical ILs, we enhanced the conversion efficiency of the R6-BDP aggregates from fluorophores to photosensitizers. The optical properties of R6-BDP in both the molecular and aggregated states were investigated through UV-visible, fluorescence and time-resolved fluorescence spectroscopy techniques. Notably, the absorption data indicated the formation of "red-shifted H-aggregates", which is an unusual phenomenon. The emission intensity of the R6-BDP aggregates decreased by approximately 65-fold compared to their molecular form, suggesting that the aggregation-caused quenching effect (ACQ) occurred in the aggregated state. The average lifetimes of the molecular and aggregate forms were estimated to be 4.52 ns and 1.02 ns, respectively. Photophysical studies suggested that the addition of a shorter alkyl chain IL (C_2C_2im-Br) promotes the formation of R6-BDP aggregates, whereas a longer alkyl chain IL (C_8C_8im-Br) induces their dissociation, returning the aggregates to their molecular form. No significant effect on aggregation was observed with the medium-length alkyl chain IL (C_4C_4im-Br). FESEM (field emission scanning electron microscopy) analysis revealed that in the presence of C_2C_2im-Br, the particle size of the R6-BDP aggregates increased, with a corresponding change in shape from round to rod-like structures. However, the particle size decreased with the addition of C_8C_8im-Br, and the particles appeared circular in shape. Theoretical density functional theory (DFT) studies provided further confirmation of the formation of H-type aggregates for the R6-BDP molecules. Biological studies revealed that the addition of a short alkyl chain IL to the R6-BDP aggregates significantly enhanced singlet oxygen generation, as evidenced by increased green fluorescence in HeLa cells under light irradiation, indicating an improvement in their photodynamic therapy (PDT) performance. The current work offers a novel approach for the research community to realize photodynamic therapy.

Received 20th May 2025,
Accepted 21st July 2025

DOI: 10.1039/d5cp01890k

rsc.li/pccp

1. Introduction

Significant attention has recently been directed toward BODIPY (4,4-difluoro-4-bora-3*a*,4*a*-diaza-*s*-indacene) dyes because of their remarkable luminescent properties.[1,2] These organic dyes exhibit high fluorescence quantum yields, sharp absorption bands and intense emission peaks across the visible to infrared range.[1–4] One of the main features of BODIPY derivatives that has garnered significant attention is their tunable fluorescence capabilities.[5,6] The wavelengths at which these dyes absorb and emit light can be adjusted as per the requirement by modifying

[a] *Department of Chemistry, National Institute of Technology, Tiruchirappalli, Tamil Nadu-620015, India. E-mail: debashis@nitt.edu, majhi.debashis91@gmail.com; Tel: +91-8594841235*
[b] *Bio-Organic Division, Bhabha Atomic Research Centre, Mumbai-400085, India*
[c] *Homi Bhabha National Institute, Mumbai-400094, India*
[d] *Department of Cellular and Molecular Cardiology, Division of Pathology, Sree Chitra Thirunal Institute for Medical Sciences and Technology, Thiruvananthapuram, Kerala-695011, India*

the structure of the BODIPY core *via* the incorporation of various functional groups. This tunable fluorescence property is highly useful to design BODIPY derivatives with specific fluorescence characteristics suitable for a variety of applications.[1,2,7–10] However, their inherently low intersystem crossing (ISC) rate makes them inefficient triplet photosensitizers (PSs), *i.e.* restricts their use as PSs in photodynamic therapy (PDT) of cancers. Consequently, research has been dedicated to increasing their triplet yields for developing efficient PDT agents based on BODIPY dyes.

The ISC rate constant (k_{ISC}) for the singlet excited state (S_m) and triplet excited state (T_n) can be written as follows:[8,11,12]

$$k_{ISC} \propto \frac{\langle T_n|H_{SO}|S_m\rangle^2}{(\Delta E_{S_m-T_n})^2} \quad (1)$$

According to this equation, k_{ISC} is proportional to the square of the spin–orbit coupling (SOC) matrix element (H_{so} represents the SOC Hamiltonian) and inversely proportional to the square of the energy gap between S_m and T_n ($\Delta E_{S_m-T_n}$). Thus, various heavy atom-attached BODIPY dyes have been synthesized, which effectively increased the SOC to enhance their photosensitizing ability.[9] However, heavy atoms enhance the dark toxicity and increase the cost and pollution, making them unsuitable for practical applications. Alternatively, heavy atom-free PSs can be synthesized by designing low $\Delta E_{S_m-T_n}$ molecules.[13] The planar conjugated BODIPY molecule has a high energy gap between the singlet and triplet excited states ($\Delta E_{S_m-T_n}$) due to the very strong spatial overlap of its molecular orbitals. Thus, the ISC process is inefficient in BODIPY, showing a very low triplet quantum yield. Various strategies have been adopted to reduce $\Delta E_{S_m-T_n}$ such as molecular twisting and generation of charge transfer states, which enhance the ISC rate.[14] Thus far, all the strategies adopted to the improve triplet yield are based on the synthetic modification of BODIPY dyes, which are tedious, time-consuming and resource intensive. Instead, new strategies that enable control of the fluorescence of BODIPY to enhance its ISC rate without synthesizing new molecules would be highly interesting. One strategy involves the formation of dye aggregates, which can help control the fluorescence properties.[15,16] The aggregation state of dye molecules causes the fluorescence intensity to decrease, suggesting that the released energy is transferred through nonradiative processes such as internal conversion and intersystem crossing. If the ISC process is enhanced, the chromophore can act as a triplet sensitizer, transferring its energy from the excited triplet state to molecular oxygen, producing singlet oxygen ($^1O_2$). Kang *et al.*[17] reported for the first time an innovative supramolecular method to transform fluorescent organic molecules into effective photosensitizers *via* aggregation. This strategy to create photosensitizers through aggregation can be helpful for PDT in cancer treatment. Based on the discussion above, the current work aimed to develop a strategy to control the fluorescence intensity of aggregated BODIPY derivatives, and also to improve the triplet conversion of BODIPY dyes, which inherently have a very low ISC conversion rate.

It is commonly known that in aqueous solution, dye molecules containing polynuclear aromatic moieties strongly prefer to form colloidal aggregates.[18] Thus, hydrophobic BODIPY dyes also have a tendency to form aggregates in water because of their intermolecular interactions and π–π stacking of the planar π conjugated BODIPY chromophore.[19] Because of the formation of different aggregate structures in the presence of water, the emission properties of the BODIPY molecule in the aggregated state in most cases are significantly quenched.[19]

According to previous reports, micelles can serve as a great medium for encapsulating hydrophobic molecules, and also can aid in making them more soluble in aqueous solutions.[20,21] The preparation of micelles commonly involves the use of surfactants such as sodium dodecyl sulphate and TRITON-X.[20,22] However, micelles have also been formed in aqueous media using surface active ionic liquids (SAILs).[20,22] Because SAILs have long alkyl chains, which give them surface-active qualities, they have low toxicity, very low vapor pressure, great thermal stability, and other desirable characteristics.[23] It has been demonstrated that SAILs can function as more efficient micelle-forming agents than traditional surfactants.[24,25] Dandpat *et al.*[26] demonstrated that SAIL can serve as an effective medium for dissociating organic aggregates. Martins and coworkers[27,28] used *N*-alkyl isoquinolinium, *N*-alkyl pyridinium, and 1-alkyl-3-methyl benzimidazolium chloride ionic liquids to induce the aggregation of asphaltene and understand the influence of these ILs on the aggregation of asphaltene. Although some reports in the literature address the impact of ILs on organic aggregates of various small drug molecules,[29,30] currently there are no reports available specifically examining their effects on BODIPY derivatives. Moreover, researchers have primarily focused on the effect of imidazolium-based asymmetrical ionic liquids on the aggregation of organic molecules,[26,28] leaving the impact of symmetrical imidazolium-based ILs unstudied. Notably, the physicochemical properties and structural organization of imidazolium-based symmetrical ILs differ significantly from that of their asymmetrical counterparts.[31–34] Therefore, it is of particular interest to investigate how symmetrical ionic liquids affect the aggregated state of BODIPY molecules. Specifically, this study aimed to explore how short and long cation alkyl-chain based symmetrical imidazolium ILs influence the aggregation state of BODIPY molecules. The van der Waals and electrostatic interactions among the ionic constituents of ILs vary with changes in their cation or anion chain length, thereby influencing both their overall properties and structural organization.[32–37] Thus, it is crucial to examine whether the cation chain length of symmetrical IL affects the formation of BODIPY aggregates.

For this purpose, we synthesized a BODIPY derivative, 2,6-diethyl-4,4-difluoro-1,3,5,7-tetramethyl-8-phenyl-4-bora-3*a*,4*a*-diaza-*s*-indacene (R6-BDP). Additionally, we prepared a series of ILs, including 1,3-diethylimidazolium bromide (C_2C_2im-Br), 1,3-dibutylimidazolium bromide (C_4C_4im-Br), and 1,3-dioctylimidazolium bromide (C_8C_8im-Br), to examine the influence of symmetrical ILs on the aggregates of R6-BDP. The molecular structures of all these compounds are provided in Chart 1.

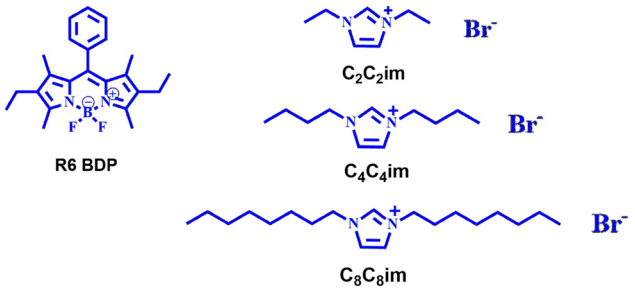

Chart 1 Chemical structures of R6-BDP, C_2C_2im-Br, C_4C_4im-Br and C_8C_8im-Br.

Initially, we examined the photophysical behavior of R6-BDP in both its molecular and aggregated forms. The effect of symmetrical ILs on the aggregation state of R6-BDP was also examined using various spectroscopic techniques, including UV-visible, fluorescence and time-resolved fluorescence spectroscopy. Their microscopic behaviors in the aggregated state, both in the presence and absence of ILs, were examined by field emission scanning electron microscopy (FESEM) and dynamic light scattering (DLS) methods. DFT-based theoretical calculations were also performed to evaluate the aggregation patterns and triplet photosensitizing properties of this molecule. Further, the singlet oxygen generation capabilities of the BODIPY dye aggregates were measured. Finally, biological studies were performed to confirm the singlet oxygen generation by the R6-BDP aggregates, both in isolation and in the presence of IL. The cytotoxicity of the R6-BDP aggregates, with and without ionic liquid, under light illumination conditions was evaluated using HeLa cells. The findings offer valuable insights into the crucial role of ILs in enhancing the PDT activity of BODIPY dyes. This information will be valuable for the practical application of ionic liquids in enhancing BODIPY-based PDT therapies for real-time cancer treatment.

2. Experimental

2.1. Materials

The compounds used for the synthesis of R6-BDP including 3-ethyl-2,4-dimethyl-1*H*-pyrrole, triethylamine, benzoyl chloride, and boron trifluoride etherate were obtained from Sigma-Aldrich. The compounds for the preparation of the ionic liquids (C_2C_2im-Br, C_4C_4im-Br, and C_8C_8im-Br) including ethyl imidazole, butyl imidazole, octyl imidazole, ethyl bromide, butyl bromide, and octyl bromide were also purchased from Sigma-Aldrich. 1,3-Diphenylisobenzofuran was used in the biological studies and obtained from Sigma-Aldrich. R6-BDP aggregates were prepared using double-distilled Milli-Q water.

2.2. Synthesis and characterisation

2.2.1. 2,6-Diethyl-4,4-difluoro-1,3,5,7-tetramethyl-8-phenyl-4-bora-3a,4a-diaza-*s*-indacene (R6-BDP)[38]. 3-Ethyl-2,4-dimethyl-1*H*-pyrrole (1.10 mL, 8.13 mmol) and benzoyl chloride (0.47 mL, 4.06 mmol) were mixed in dry dichloromethane (25 mL) in a Schlenk flask under an argon (Ar) atmosphere, and then the reaction mixture was stirred for 24 h at 25 °C. Then the mixture was ice-cooled and triethyl amine (5.66 mL, 40.6 mmol) was slowly added to it and stirred for 15 min. After that, boron trifluoride etherate ($BF_3{\cdot}OEt_2$) (6.0 mL, 48.72 mmol) was slowly added to this solution and the resultant mixture was stirred for 24 h at 25 °C. Then, the reaction was quenched with 50 mL of saturated aqueous sodium bicarbonate solution, extracted with 3 × 75 mL of dichloromethane, washed with 3 × 50 mL of water and 50 mL of brine and dried with Na_2SO_4. The organic mixture was concentrated *in vacuo* to obtain and the crude product, which was purified by flash column chromatography (silica gel, DCM/petroleum ether, 50 : 50) to furnish the R6-BDP (385 mg, 50%) dye as a brick red solid. The compound was characterised by ^{1}H and ^{13}C NMR spectroscopy (Fig. S1 and S2).

^{1}H NMR (500 MHz, $CDCl_3$): δ (ppm) 7.47–7.46 (m, 3H), 7.29–7.27 (m, 2H), 2.53 (s, 6H), 2.30 (q, J = 7.5 Hz, 4H), 1.27 (s, 6H), 0.98 (t, J = 7.5 Hz, 6H).

^{13}C NMR (125 MHz, $CDCl_3$): δ (ppm) 153.7, 140.2, 138.4, 135.8, 132.7, 130.8, 128.9, 128.7, 128.3, 17.1, 14.6, 12.5, 11.6.

2.2.2. 1,3-Dialkyl imidazolium bromide ($C_nC_n$im-Br). The ionic liquids, 1,3-dialkyl imidazolium bromide ($C_nC_n$im-Br, where n = 2, 4, 8), were synthesized by following the reported procedures.[31,39] To synthesize $C_nC_n$im-Br, 1-alkyl-imidazole (1.0 mmol) was added to 30 mL of acetonitrile in an RB (round-bottom) flask and the mixture was stirred. Then, 1-bromoalkane (1.10 mmol) was added dropwise to the reaction mixture. The mixture was refluxed under a nitrogen atmosphere for 72 h. The reaction mixture was concentrated *in vacuo* and the oily product was washed 5–6 times with diethyl ether, yielding a colorless liquid. Then, the compounds were dried under vacuum for two to three days to remove any water and ensure the high purity of the ILs. Characterization of the ILs was carried out using ^{1}H NMR spectroscopy, along with mass spectrometry (Fig. S3–S8).

C_2C_2im-Br: ^{1}H NMR (500 MHz, DMSO-d_6): δ (ppm) 9.48 (s, 1H), 7.90 (d, 2H), 4.22 (q, 4H), 1.41 (t, 6H).

ESI-MS (+ve): 125 *m*/*z*, $[C_2C_2im]^+$

C_4C_4im-Br: ^{1}H NMR (500 MHz, DMSO-d_6): δ (ppm) 9.45 (s, 1H), 7.88 (d, 2H), 4.21 (t, 4H), 1.78 (m, 4H), 1.24 (m, 4H), 0.88 (t, 6H).

ESI-MS (+ve): 181 *m*/*z*, $[C_4C_4im]^+$

C_8C_8im-Br: ^{1}H NMR (500 MHz, DMSO-d_6): δ (ppm) 9.61 (s, 1H), 7.95 (d, 2H), 4.23 (t, 4H), 1.79 (m, 4H), 1.20 (m, 20H), 0.81 (t, 6H).

ESI-MS (+ve): 293 *m*/*z*, $[C_8C_8im]^+$

2.3. Preparation and characterization of R6-BDP aggregates

The preparation of R6-BDP aggregates was studied using the conventional re-precipitation method.[40,41] Usually, 30 μL of R6-BDP solution (0.01 M) in acetonitrile was quickly added to water (3 mL) under sonication. After 20 min of continuous stirring, colloidal aggregates were formed. The formation of R6-BDP aggregates was confirmed by characterizing the freshly prepared solution using UV-visible absorption, FESEM and DLS.

2.4. Instrumentation and methods

The ^{1}H and ^{13}C NMR spectroscopic techniques were performed using a Bruker Avance NMR (500 MHz) spectrometer, with tetramethylsilane (TMS) serving as the internal standard. An Agilent QTOFG6545 spectrometer was used to obtain high-resolution mass spectrometry data at a resolution of 50 000 in ESI mode. A JASCO V-750 spectrophotometer was used to record all the steady-state absorption spectra, while fluorescence spectra were obtained with a JASCO FP-8200 spectrofluorometer. Time-resolved fluorescence studies were performed using a DeltaFlex time correlated single photon counting (TCSPC) spectrometer from HORIBA. The probe was excited by a laser diode source (λ_{exc} = 500 nm, FWHM = 81 ps) and an HPPD (HORIBA) detector was used. The EzTime decay analysis software was used to evaluate the fluorescence intensity decay through a non-linear least square's iteration process. The χ^2 (chi square) values were used to assess the fit quality, and fitting was used to determine the weighted deviation. Origin 8.0 was used for the plotting and analysis of all data. R6-BDP aggregates, with and without ILs, were analysed *via* imaging using a ZEISS FESEM.

2.5. Computational methods

The ground-state structures of R6-BDP in both the monomer and dimer were optimized to gain insight into the inter and intra-molecular interactions of R6-BDP, which helps to understand the aggregation behavior of the R6-BDP molecule. The optimization of the R6-BDP molecule was performed using density functional theory (DFT) calculations employing the B3LYP functional and the 6-31+G(d,p) basis set, as implemented in the Gaussian 09 software.[42,43] The ground-state geometries of the R6-BDP molecules and dimer of the R6-BDP molecule were initially optimized using DFT in acetonitrile, and then time-dependent DFT (TD-DFT)[44] was used to simulate the absorption (excitation) spectra.

2.6. Singlet oxygen ($^{1}O_2$) generation

To detect singlet oxygen ($^{1}O_2$) in various solutions, 1,3-diphenylisobenzofuran (DPBF) was employed as a chemical probe. Solutions of molecular R6-BDP, aggregate form, and R6-BDP aggregates with ionic liquid were each dispersed in 1 mL of an aqueous solution containing 60 μM DPBF. Subsequently, the mixtures were transferred to a cuvette and exposed to monochromatic light. Changes in absorption at 410 nm were monitored using a UV-vis absorption spectrophotometer.

2.7. Cell culture

The human cervical cancer cell line (HeLa) was maintained in Dulbecco's modified Eagle medium (DMEM) supplemented with 10% fetal bovine serum (FBS) and 10% antibiotic–antimycotic solution in a CO_2 incubator at 37 °C. The cells were cultured in 60 mm dishes until reaching approximately 80% confluence.

2.8. Cell viability assay

The viability of the HeLa cells was measured by means of the MTT ((3-[4,5-dimethylthiazol-2-yl]-2,5-diphenyl tetrazolium bromide) assay. Briefly, the cells were seeded (1×10^4 cells per well) in 96-well plates and maintained in a CO_2 incubator at 37 °C for 24 h. At approximately 80% confluence, the compound R6-BDP aggregates and aggregated form $+C_2C_2$im-Br were added at 0.2 μM, 2 μM, 4 μM and 8 μM concentrations, respectively. After two hours of incubation in the dark, one set was exposed to LED for 5 min. Then, the plates were incubated overnight at 37 °C in a CO_2 incubator. MTT (0.5 g L^{-1}) was added to each well, as described previously by Mosmann[45] to estimate mitochondrial dehydrogenase activity. After 4 h incubation, DMSO was added to each well to solubilize the MTT formazan crystals and the absorbance was recorded at 570 nm. The outcomes were reported as the percentage of cytotoxicity.

$$\text{Percentage toxicity} = \frac{(\text{Absorbance of control} - \text{Absorbance of sample})}{\text{Absorbance of control}} \times 100$$

2.9. Measurement of intracellular reactive oxygen species

Briefly, cells were seeded (1×10^4 cells per well) in black glass-bottom 96-well plates (BD Bioscience, USA) and incubated in a CO_2 incubator for 24 h at 37 °C. At approximately 80% confluence, the compound aggregated form of R6-BDP and aggregated form $+C_2C_2$im-Br were added at 0.2 μM, 2 μM, 4 μM and 8 μM concentrations, respectively. After 2 h of incubation in the dark, one set was exposed to an LED light for 5 min. The plates were incubated overnight in a CO_2 incubator. Reactive oxygen species (ROS) in HeLa cells were evaluated by utilizing a fluorescent probe, DCFH-DA, as reported previously by Cathcart *et al.*[46] Briefly, the cells were incubated with DCFH-DA (20 μM) in PBS (pH 7.4) for 20 min. After washing with PBS, the cells were imaged using a fluorescence microscope (Olympus IX83) equipped with FITC filters (excitation at 490 nm and emission at 525 nm). Fluorescence intensity was determined using the cellSens program.

3. Results and discussion

3.1. Photophysical studies of R6-BDP in molecular and aggregated form

The photophysical properties of R6-BDP were initially examined in both its molecular and aggregated forms. The absorption spectra of R6-BDP in both forms are presented in Fig. 1(a), while Table 1 summarizes the corresponding data. As seen in Fig. 1(a), a sharp absorption band was observed at approximately 522 nm in the molecular form, with a shoulder absorption band appearing at around 491 nm. The sharp absorption in the visible region is attributed to the $0 \rightarrow 0$ vibronic band for the $S_0 \rightarrow S_1$ transition, while the shoulder corresponds to the $0 \rightarrow 1$ vibronic band for the same transition. It is worth mentioning that similar types of absorption bands have been

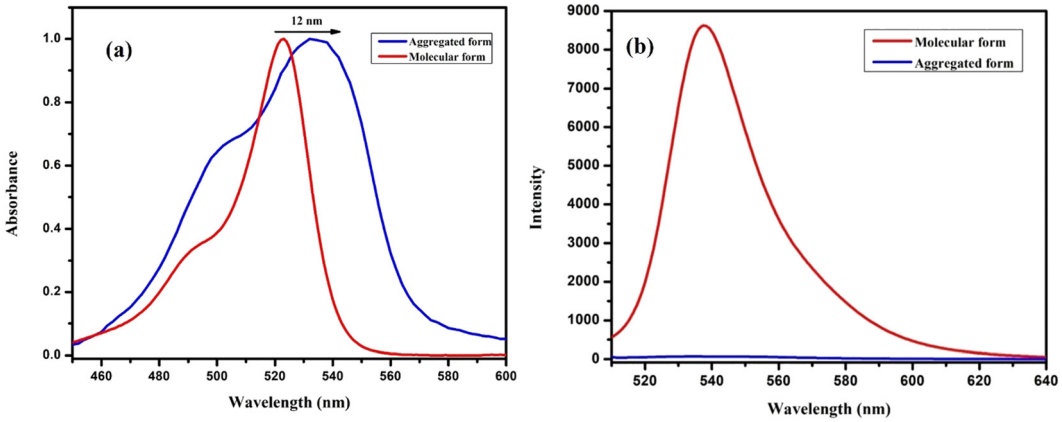

Fig. 1 (a) Normalised absorption and (b) emission spectra of R6-BDP in the molecular and aggregated form.

Table 1 Absorption (λ_{abs}^{max}) and emission (λ_{em}^{max}) maxima of R6-BDP in its molecular and aggregated forms

R6-BDP	Absorption (λ_{abs}^{max}) (nm)	Emission (λ_{em}^{max}) (nm)
Molecular form	522 ± 2	536 ± 2
Aggregated form	534 ± 2	560 ± 2

published by other researchers when examining the absorption spectra of BODIPY molecules.[8] Similar to its molecular form, the absorption profile of R6-BDP in the aggregated form displayed a sharp peak near 534 nm and a shoulder at around 502 nm (Fig. 1(a)).

Again, the absorption maximum of R6-BDP in its aggregated form is red shifted by over 12 nm compared to its corresponding molecular form, as shown in Fig. 1(a). According to Kasha's theory, molecular aggregates are classified as J or H aggregates depending on whether their absorption spectrum is red or blue shifted compared to their molecular form.[47] Thus, the observed red shift in the absorption spectrum indicates the formation of J-type aggregates for the R6-BDP molecule. However, some recent reports in the literature suggest that the red shift in the absorption spectrum is not necessarily induced by J-aggregation, but rather by the coupling of excitons and vibrations.[38] Spano *et al.*[48,49] demonstrated that the type of aggregation is independent of the absorption spectral shift. Instead, it is determined by the ratio of the absorbance intensities of the first two vibrational bands, A_1 and A_2, corresponding to the $0 \rightarrow 0$ and $0 \rightarrow 1$ transitions, respectively.[48,49] Again IA_1 denotes the absorption intensity of the $0 \rightarrow 0$ vibronic band, and IA_2 denotes the absorption intensity of the $0 \rightarrow 1$ vibronic band (Table 2). The decrease in the ratio of absorption intensities of these two vibronic bands in the aggregated state, which is related to the molecular state of R6-BDP, shows the formation of H-type aggregates.[48,49]

Table 2 Absorption position of vibronic bands and change in their intensity ratio

R6-BDP	A_1 position (nm)	A_2 position (nm)	IA_1/IA_2	% change
Molecular form	522	491	2.941	48%
Aggregated form	534	502	1.508	

The absorption intensity ratio of the first two vibronic bands for both the molecular and aggregated forms is provided in the Fig. S9, with the corresponding data given in Table 2. The data demonstrates a significant reduction in the ratio of the first two vibronic bands from the molecular to aggregated form of R6-BDP, indicating that the aggregates are predominantly H-aggregates. Interestingly, the investigation revealed that the aggregates of R6-BDP exhibit non-Kasha's behaviour, *i.e.* "red shifted H-aggregates", which is quite uncommon (Fig. 2). The formation of "red-shifted H-aggregates" is propelled by the substantial quadrupole–quadrupole interaction.[50] These aggregates exhibit all the typical features of H-aggregates, such as suppressed radiative decay rates and vibronic signatures in their absorption and emission spectra, consistent with the Frenkel exciton models, except for the red shift in their absorption peak.[50]

To gain more insight into the excited-state properties of both the molecular and aggregated forms, we performed fluorescence spectroscopy. The emission spectra of R6-BDP in molecular and aggregated form are shown in Fig. 1(b) and data are listed in Table 1. Similar to the absorption spectra, the

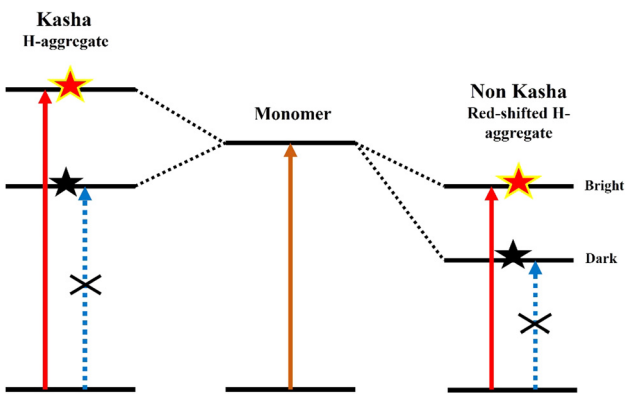

Fig. 2 Schematic of the allowed transitions for the H-aggregate (Kasha) and red-shifted H-aggregate (non-Kasha).

emission maximum (λ_{em}^{max}) of the R6-BDP molecules upon photoexcitation at 500 nm shifted towards longer wavelengths (red shift) by 24 nm in the aggregated state relative to the molecular form. However, the emission intensity in the aggregated state of R6-BDP was significantly quenched compared to the molecular form of R6-BDP. In fact, the fluorescence intensity decreased by approximately 65-fold in the aggregated state relative to the molecular form due to the aggregation-caused quenching (ACQ) phenomenon (Fig. 1(b)). Several factors may contribute to the reduced fluorescence intensity in the aggregated state. One factor is the ACQ effect likely occurring due to a change in the emitting state upon aggregation.[51] This effect is driven either by the strong π–π coupling of the planar π-conjugated structures of BODIPY molecules, which results in the formation of excimers or exciplexes, or by collisions between the excited and ground states of the fluorescent molecules at relatively high concentrations, resulting in non-radiative deactivation.[52]

To gain a better understanding of the ACQ effect, we performed time-resolved fluorescence lifetime measurements of R6-BDP in both the molecular and aggregated states. The fluorescence lifetime data for both forms are provided in Table 3. Notably, the fluorescence intensity decay of the molecular form was best fitted by a mono-exponential model, while the aggregated form followed a tri-exponential decay. The tri-exponential fitting parameters for the aggregated form are provided in the Table S1. The fluorescence lifetimes of the molecular and aggregated forms of R6-BDP were estimated to be 4.54 ns and 1.02 ns, respectively. The data clearly indicate that the lifetime values are significantly lower in the aggregated state than in the molecular form, further supporting the ACQ phenomenon in the excited state.[48,53]

3.2. Effect of symmetrical ionic liquids on the R6-BDP aggregates

Over the past few years, researchers have thoroughly examined the development of very stable and organized supramolecular assemblies using oppositely charged surfactants. Thereafter, to create different supramolecular aggregates, the surfactants were replaced by surface-active ionic liquids, a unique family of ILs.[26–28,54] As a result, the structural elements of supramolecular aggregates-vesicular assemblies, micelles and mixed micelles have been altered from the oppositely charged SAIL/SAIL pair to surfactant/surfactant and surfactant/SAIL pairs.[26–28,54] The most recent addition to this ion pair combination are dye molecules with a hydrophilic ionic head group and a lengthy hydrophobic chain segment.[26–28,54] Hence, SAIL/dye or surfactant/dye pairs can also lead to the formation of different assemblies through electrostatic, hydrophobic or π–π stacking.[26–28,54] It is important to note that the chain length of the cation or anion in various ionic liquids plays a critical role in determining their properties.[26,27] By altering the chain length, the electrostatic and van der Waals forces among the components of the ionic liquids can be modified.[25,26] For instance, ILs with long alkyl chains, such as 1-dodecyl imidazole, exhibit behavior typical of surfactant-active ionic liquids (SAILs),[26] whereas ILs with very short alkyl chains do not display this behavior.[55] Therefore, it is crucial to investigate how ionic liquids with varying alkyl chain lengths influence the aggregate states of a drug molecule.

Table 3 Average lifetime data for the molecular, aggregated and ionic liquids added to the aggregated form of R6-BDP

System	Average lifetime (ns)	Chi square (χ^2)
Molecular form	4.54 ± 0.23	1.05
Aggregated form	1.02 ± 0.05	1.18
Aggregated form + C_2C_2im-Br	1.00 ± 0.05	1.05
Aggregated form + C_4C_4im-Br	1.07 ± 0.05	1.02
Aggregated form + C_8C_8im-Br	5.12 ± 0.26	1.04

3.2.1. Effect of short alkyl chain ionic liquid. The effect of short alkyl chain ionic liquids on the aggregates of R6-BDP was investigated by gradually adding the cationic short alkyl chain IL C_2C_2im-Br. Fig. 3(a) shows the absorption spectra of the R6-BDP aggregates in the presence and absence of C_2C_2im-Br. As seen in Fig. 3(a), the absorption spectra shifted towards longer wavelengths (red shift), and the absorption intensity decreased upon the addition of C_2C_2im-Br to the R6-BDP aggregates. Interestingly, the absorption spectra became broadened as the concentration of C_2C_2im-Br increased. The FWHM (full width at half maximum) values of the absorption spectra for the R6-BDP aggregates and R6-BDP aggregates in the presence of 164.5 μM C_2C_2im-Br were determined to be 62 nm and 157 nm, respectively. The FWHM values suggest that the absorption spectra broadened significantly upon the addition of C_2C_2im-Br. The red shift and broadening of the absorption peaks in the presence of C_2C_2im-Br suggest that the addition of the short alkyl chain IL caused the R6-BDP aggregates to transition towards a more solidified form. Due to the presence of a small hydrophobic alkyl chain in C_2C_2im-Br, electrostatic interactions may dominate over van der Waals forces, causing the short alkyl chain ionic liquid to behave like a pure salt. This salt-like nature of C_2C_2im-Br facilitated the formation of organic aggregates of R6-BDP molecules. In this context, it is worth noting that Christau and coworkers[56] previously reported the salt-induced aggregation of citrate-coated gold nanoparticles (AuNPs) enclosed inside poly(N isopropyl-acrylamide) brushes implanted from plain substrates. They found that salt-induced AuNP aggregation resulted in nanoparticle assemblies that varied depending on the type of salt.[56] Thus, it is intriguing that short alkyl chain ionic liquids can behave like a salt,[57] which facilitates the formation of aggregates of R6-BDP molecules.

Our interpretation of the mechanism of the absorption intensity quenching is further supported by the emission spectroscopy data for the R6-BDP aggregates. Quite interestingly, the fluorescence intensity of the R6-BDP aggregates gradually decreased with an addition of C_2C_2im-Br, as shown in Fig. 3(b). The broadening in the emission spectra and decrease in emission intensity upon the gradual addition of the short alkyl chain IL indicate that R6-BDP molecules were tending towards the solid form. The decrease in fluorescence

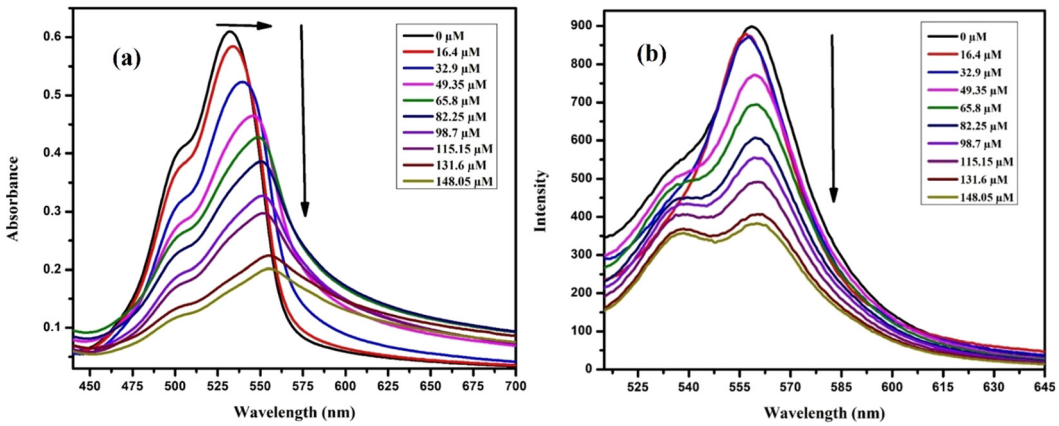

Fig. 3 (a) Absorption and (b) emission spectra of the aggregated state of R6-BDP with gradual addition C_2C_2im-Br.

intensity is primarily attributed to the intermolecular vibronic interactions, causing the nonradiative deactivation process, which possibly involves internal conversion, ISC or fluorescence quenching such as excitonic coupling and excimer formation.[17] Enhancing the ISC process ($S_1 \rightarrow T_n$) upon aggregation could allow the R6-BDP to act as a sensitizer, transferring its triplet excited state energy to molecular oxygen, thereby generating singlet oxygen ($^1O_2$), which would be very helpful for PDT.[17] The generation of singlet oxygen in R6-BDP aggregates in the presence of C_2C_2im-Br is confirmed and discussed in Section 3.5.

Furthermore, the fluorescence quenching of the R6-BDP aggregates by C_2C_2im-Br was analysed using the Stern–Volmer plot.[58] This plot, which shows the relationship between F_0/F and C_2C_2im-Br concentration, is presented in Fig. 4. Based on the linear fit of the Stern–Volmer plot,[58] the quenching process appears to be either exclusively static or dynamic in nature (see Fig. 4). To distinguish whether the observed quenching behaviour is due to a static or dynamic process, fluorescence decay measurements of the R6-BDP aggregates in presence of C_2C_2im-Br were conducted using the TCSPC technique.

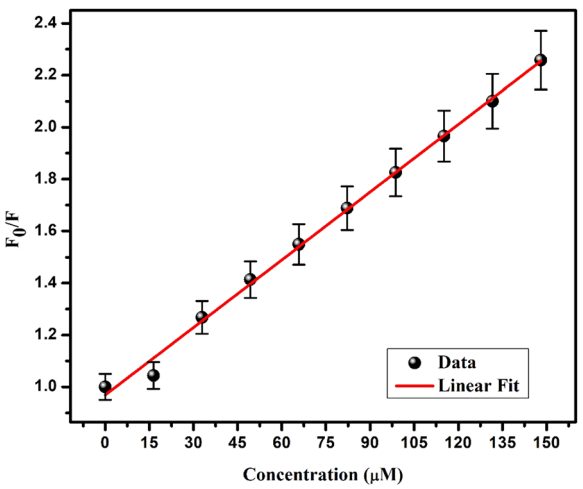

Fig. 4 Stern–Volmer plot illustrating the changes in the fluorescence intensity of R6-BDP aggregates with varying concentrations of the ionic liquid (IL). The black lines represent the error bars for the data points.

The representative fluorescence decay profiles of the R6-BDP aggregates, both with and without C_2C_2im-Br, are shown in Fig. 5, with the corresponding data provided in Table 3. The average lifetime values of the R6-BDP aggregates in the absence and presence of C_2C_2im-Br are 1.02 ns and 1.00 ns, respectively. These results suggest that the fluorescence lifetime of the R6-BDP aggregates did not change significantly upon the addition of the short alkyl chain IL, indicating that the quenching mechanism is purely static in nature.

3.2.2. Effect of medium and long alkyl chain ionic liquids. Further, we examined the effect of medium alkyl chain IL on the R6-BDP aggregates using a medium cationic alkyl chain symmetrical IL, C_4C_4im-Br. The absorption spectra of the R6-BDP aggregates with and without C_4C_4im-Br are presented in Fig. S10(a). Both the absorption intensity and absorption maxima of the R6-BDP aggregates did not change significantly upon the addition of C_4C_4im-Br as shown in Fig. S10(a). To better understand the role of C_4C_4im-Br, we also performed fluorescence spectroscopy. Fig. S10(b) represents the emission spectra of the R6-BDP molecules in aggregated form in the presence of C_4C_4im-Br. Similar to absorption, no significant changes in the emission maxima and emission intensity were observed for the R6-BDP aggregates upon the addition of C_4C_4im-Br. The data suggest that C_4C_4im-Br had no effect on the R6-BDP aggregates. This might be because it is a medium hydrophobic alkyl chain ($n = 4$) ionic liquid, which does not behave like a pure salt or it cannot form micelles[57] because both the electrostatic interaction and van der Waals interaction among the IL components may be balanced.

Moreover, to confirm this, we performed time-resolved fluorescence lifetime measurements. The average lifetime for the aggregated form and in the presence of C_4C_4im-Br was found to be 1.02 and 1.07, respectively (Table 3), which indicates that the change in fluorescence lifetime is not significant. This investigation suggests that medium alkyl chain ionic liquids do not have much effect on organic aggregates of R6-BDP.

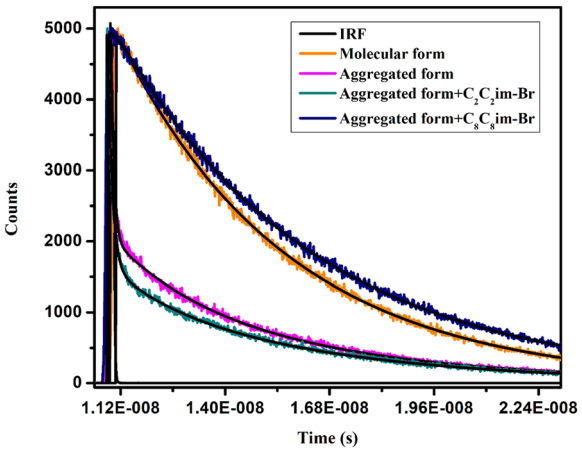

Fig. 5 Fluorescence intensity decay profile of R6-BDP in the molecular form, aggregated form, and R6-BDP aggregates in the presence of C_2C_2im-Br and C_8C_8im-Br. Black lines represent the fitted data points.

Additionally, we extended our studies by using a longer cationic alkyl chain ionic liquid, C_8C_8im-Br, to investigate its effect on the R6-BDP aggregates. The representative absorption spectra of the R6-BDP aggregates, both with and without C_8C_8im-Br, are presented in Fig. 6(a). Upon the gradual addition of C_8C_8im-Br, the absorption intensity of the R6-BDP aggregates sharply increased and their absorption maximum shifted towards the shorter wavelength region (blue shift), as shown in Fig. 6(a). The observed increase in absorption intensity and the blue shift in absorption maximum indicate the dissociation of the aggregate molecules, transitioning towards a molecular form. Furthermore, we also performed a fluorescence study on the R6-BDP aggregates with the gradual addition of a longer alkyl chain IL (Fig. 6(b)). The addition of C_8C_8im-Br to the aggregated solution of R6-BDP was observed to cause a hypsochromic shift in its emission spectrum and its emission intensity increased by around 26-fold. This behaviour is likely due to the longer alkyl chain in C_8C_8im-Br, which enhances the hydrophobic interaction over the electrostatic interaction, thereby favouring the formation of micelles in the aqueous solution.[53] The significant blue shift in the emission spectrum and the increased emission intensity of the R6-BDP aggregates in the presence of C_8C_8im-Br suggest that the dissociated species are highly stable within the hydrophobic core of the micelles. The data also suggest that the R6-BDP aggregates dissociate and transition towards the molecular form in the presence of C_8C_8im-Br. This occurs due to the micellar effect of the longer alkyl chain IL. The presence of a long hydrophobic chain (n = 8) in C_8C_8im-Br allows greater compactness, enabling it to easily form micelles above its critical micelle concentration.[57] To determine the critical micelle concentration (CMC) value, we plotted a graph of fluorescence intensity *versus* the concentration of C_8C_8im-Br (Fig. S11). The inflection point of the sigmoidal curve in the graph is found to be approximately 10.3 μM, indicating that micelle formation occurred after the addition of 10.3 μM C_8C_8im-Br. This is due to the formation of micelles, which help in encapsulate the aggregates of R6-BDP molecules and break their aggregation.

To gain further insights into the increase in the fluorescence intensity of the R6-BDP aggregates, we also performed time-resolved fluorescence lifetime measurements. The fluorescence decay profile depicting the effect of a longer alkyl chain ionic liquid (C_8C_8im-Br) on the aggregates of R6-BDP is shown in Fig. 5. The fluorescence decay trace (excited at 500 nm) was fitted to triexponential functions. The lifetime value increased from τ = 1.02 ns to τ = 5.12 ns upon the addition of a longer alkyl chain ionic liquid (C_8C_8im-Br) to the R6-BDP aggregates, which is close to that of the molecular form of R6-BDP. This signifies that the aggregation was broken and it was tending towards the molecular form. The dissociation of aggregates into monomers is a key factor in enhancing the activity of drugs in biological systems, which makes this an intriguing observation.[26] Interestingly, the effect of the long alkyl chain IL significantly differed from that of the short alkyl chain IL. The short alkyl chain IL had the tendency of inducing aggregation, which we discussed earlier (Section 3.2.1). In contrast, the longer alkyl chain IL can able to form molecular species (Fig. 7). A dramatic colour change from pale pink to lime green under UV light was observed upon the addition of the longer alkyl chain IL (C_8C_8im-Br) to the R6-BDP aggregates, as shown in

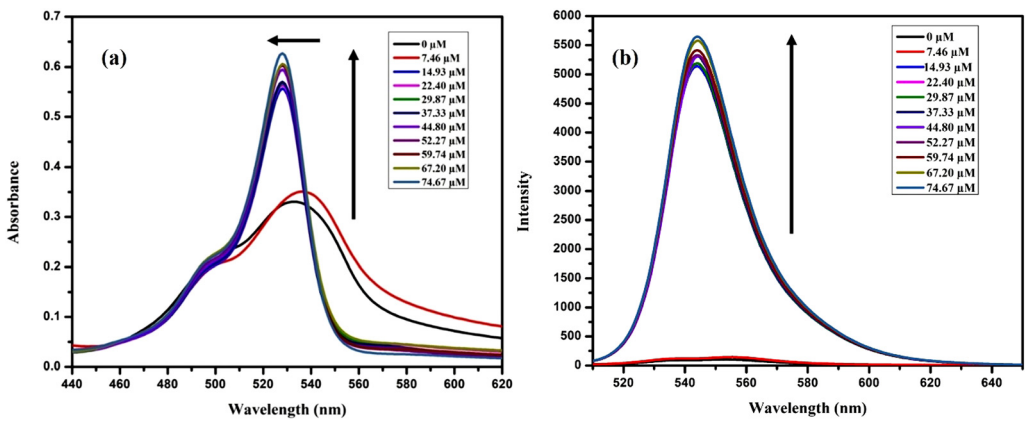

Fig. 6 (a) Absorption and (b) emission spectra of aggregated state of R6-BDP with the gradual addition of C_8C_8im-Br.

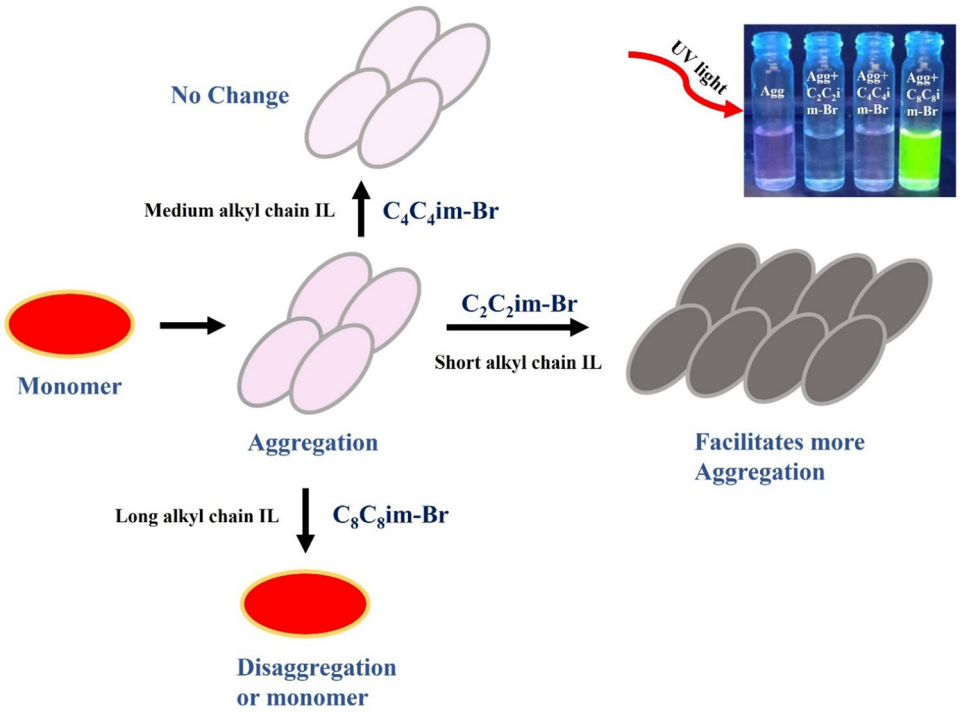

Fig. 7 Schematic of the self-assembly of R6-BDP upon the addition of C_2C_2im-Br, C_4C_4im-Br and C_8C_8im-Br.

Fig. 7. In contrast, no colour change occurred when a medium alkyl chain ionic liquid (C_4C_4im-Br) was added to the R6-BDP aggregates. Interestingly, the colour transitioned completely from pale pink to colourless upon the addition of a short alkyl chain IL (C_2C_2im-Br) to the R6-BDP aggregates. Based on the above discussion, we conclude that the cationic alkyl chain length of symmetrical ILs plays a vital role in determining whether they facilitate the formation of organic aggregates or break them down into molecular forms. This strategy is particularly interesting given that it facilitates the formation of organic aggregates through the addition of short alkyl chain ILs, while also enabling their breakdown with the addition of long alkyl chain ILs. To further confirm our experimental observations, we extended our studies through microscopic analysis.

3.3. Microscopic analysis of R6-BDP aggregates

To examine the morphology of the R6-BDP aggregates with and without ionic liquids, FESEM images were captured at ambient temperature (Fig. 8). The estimated particle size of the R6-BDP aggregates was found to be nearly 1.518 μm and the particles were round in shape with a rough surface (Fig. 8(a)). In the presence of the shorter alkyl chain IL, the particle size of the R6-BDP aggregates increased from 1.518 μm to 7.226 μm, with a corresponding change in shape from round to rod-like structures (Fig. 8(b)). These findings strongly support the previous observations from the photophysical studies (see Section 3.2.1), which indicated that the shorter alkyl chain IL promoted the formation of R6-BDP aggregates. Furthermore, the rod-shape structure of the R6-BDP aggregates in the presence of

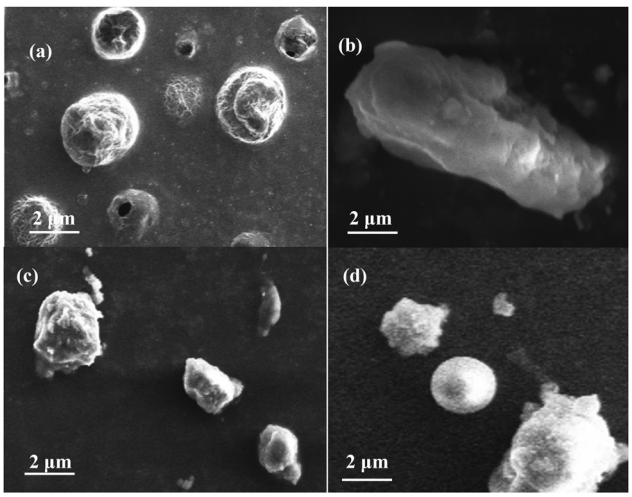

Fig. 8 FESEM images of the (a) aggregation of R6-BDP. (b) Addition of C_2C_2im-Br to the aggregation of R6-BDP. (c) Addition of C_4C_4im-Br to the aggregation of R6-BDP. (d) Addition of C_8C_8im-Br to the aggregation of R6-BDP.

C_2C_2im-Br also confirmed that R6-BDP tended towards a more solidified structure in the presence of C_2C_2im-Br. However, the particle size of the R6-BDP aggregates was found to be around 2 μm, with no noticeable change in shape upon the addition of the medium alkyl chain ionic liquid. These findings suggest that C_4C_4im-Br had no substantial effect on the R6-BDP aggregates. Interestingly, the particle size of the R6-BDP aggregates declined from 1518 nm to 209 nm with the addition of the longer alkyl chain IL (C_8C_8im-Br). Additionally, the shape of the

particles changed, becoming circular (Fig. 8(d)). This data indicates that the R6-BDP aggregates tended towards a molecular form in presence of C_8C_8im-Br. The results support the observations obtained from the spectroscopic investigation of the effect of the medium and long alkyl chain ILs on the R6-BDP aggregates (see Section 3.2.2).

Additionally, to confirm the size of the particles obtained by FESEM, dynamic light scattering measurements were also performed for all these samples. The size distribution plots of the R6-BDP aggregates, both with and without liquids, are given in Fig. S12. It was observed that the size of the particle increased from 1557 nm to 2506 nm in the presence of the shorter alkyl chain ionic liquid (C_2C_2im-Br). Additionally, the polydispersity index (PDI) increased from 0.73 to 1.26 in the presence of C_2C_2im-Br, indicating that the particles grew in size with the addition of the short alkyl chain IL. This suggests that the R6-BDP molecules form larger aggregates in the presence of short chain ILs. However, on the addition of the medium alkyl chain IL (C_4C_4im-Br), the particle size changed from 1557 nm to 1799 nm. The PDI value also increased from 0.73 to 0.88, which is not significantly different for the change upon the addition of C_4C_4im-Br. Interestingly, the size of the particles decreased from 1557 nm to 528 nm and the PDI value also changed from 0.73 to 0.01 in the presence of the longer alkyl chain IL (C_8C_8im-Br), indicating the formation of molecular form. Similar observations were previously recorded based on FESEM data.

3.4. Theoretical calculations of the experimental results

The photophysical and aggregation behavior of molecules can be better understood by using theoretical calculations.[42,43] The ground-state structures of R6-BDP, including monomers, linear dimer and B–F···H linear dimers were completely optimized in the gas phase. Theoretical calculations were performed at the DFT level with the Gaussian 09 quantum mechanical package, employing the B3LYP functional in combination with the 6-31+G(d,p) basis set. The time-dependent DFT (TD-DFT)[44] formalism was used to estimate the excitation energies at the TD-B3LYP/6-31+G(d,p) level of theory.

The self-assembled structure of R6-BDP was studied by optimizing its monomer, linear dimers and B–F···H linear dimers to help understand its aggregation behaviour, as shown in Fig. 9. As seen in Fig. 9(c), two R6-BDP molecules are connected *via* B–F···H hydrogen bonding. In this case, the two molecules are interlinked through a head-to-head fashion. The hydrogen bond distance between B–F···H is 2.19 Å, indicating strong hydrogen bonding interaction. This hydrogen bond linkage further supports the assembly of H-type aggregates of the R6-BDP molecules, consistent with the experimental observations.

The excited-state energy difference was calculated for both the monomer and dimer of R6-BDP. Fig. 10 represents the energy gap between the singlet (S_1) and triplet (T_1) energy states for both the monomer and dimer of R6-BDP. According to Kasha's rule, when the S_1 state is populated either through direct photoirradiation or *via* internal conversion from higher

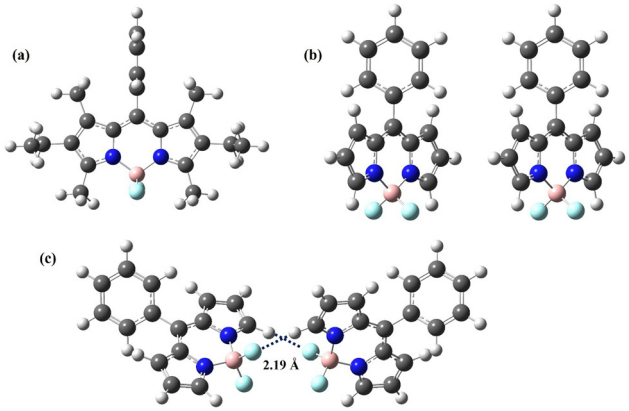

Fig. 9 Optimized geometries of R6-BDP, (a) monomers, (b) linear dimers, and (c) B–F···H linear dimers.

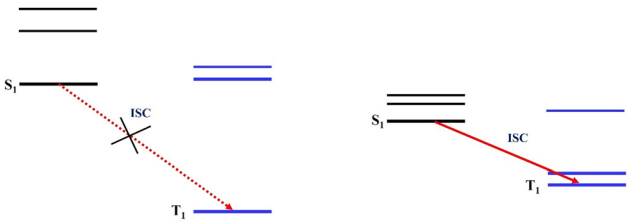

Fig. 10 Energy level illustrations for the excited singlet (black) and triplet (blue) states calculated using TD-DFT for the R6-BDP monomer (left) and dimer (right) structures.

excited singlet states, it is difficult for the monomer to transition from the S_1 state to the T_1 state because of the significant energy difference of 1.2786 eV between them, as shown in Fig. 10. Interestingly, in the dimer, the associated S_1–T_1 and S_1–T_2 energy difference is significantly reduced to 1.0758 eV and 1.0749 eV, respectively (see Table S2). According to the energy gap law,[59] inter system crossing (ISC) is more efficient when the singlet and triplet states have similar energy levels. However, based on the classical Marcus theory, the rate constants for ISC are inversely proportional to the square of the pertinent energy difference (ΔE) and directly proportional to the square of the spin–orbit coupling (H_{if}).[60] Given that heavy atom-free organic systems often have small spin–orbit couplings, the energy differences become the key factor governing the ISC efficiency.[61] Thus, the reduction in the energy gap between the S_1 and T_1 states may account for the aggregation-induced increase in the ISC efficiency observed in the present study, as discussed *vide infra*.

The computed λ_{max} values (Fig. 11) for the R6-BDP monomer and dimer forms are presented in Table 4. The calculated λ_{max} values for the monomer and dimer were found to be 448.68 nm and 456.81 nm, respectively. Although these values differ significantly from the experimental absorption maxima, both approaches show a consistent trend, *i.e.*, a red shift in the absorption spectrum upon aggregation. Notably, similar discrepancies between the theoretical and experimental

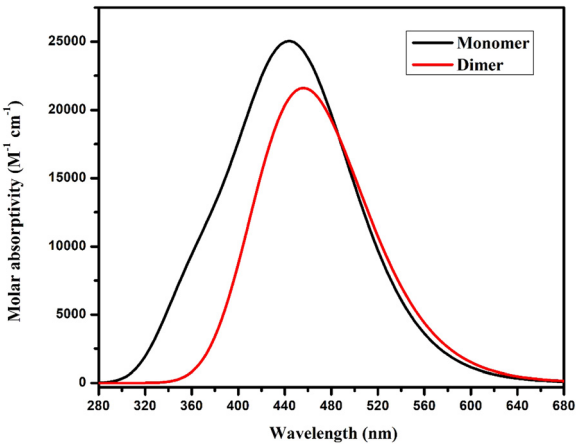

Fig. 11 Computed λ_{max} for the R6-BDP monomer and dimer at the TD-B3LYP/6-31+G(d,p) level of theory.

Table 4 Computed λ_{max} for the monomer and dimer forms of R6-BDP

System	λ_{max} (nm)	f (Oscillator strength)	Transitions
Monomer	448.68	0.586	H–L; 94.54% H-1–L; 5.45%
Dimer	456.81	0.020	H–L; 64.59% H-1–L-1; 35.41%

absorption maxima for both the molecular and aggregated forms have been reported previously.[40,62,63] These studies also emphasize that although the absolute values may vary, the observed trends remain consistent. Again, the S_0–S_1 transition is referred to as an optical transition. The theoretical results indicate that the hydrogen bonding between the R6-BDP molecules is primarily responsible for the observed red shift of 8.13 nm upon dimer formation. Furthermore, the fluorescence intensity is directly proportional to the oscillator strength (f).[64] The R6-BDP monomer exhibits a stronger oscillator strength than the dimer (Table 4), suggesting that the monomer has a higher fluorescence intensity than the dimer. Both findings align well with the experimental results.

3.5. Singlet oxygen ($^1O_2$) generation and photostability

As discussed earlier in Section 3.2.1, the shorter alkyl chain ionic IL (C_2C_2im-Br) facilitates the formation of more solidified structures of R6-BDP aggregates by promoting their aggregation. This helps in decreasing the energy gaps among the singlet and triplet excited states, as proven by the theoretical study (see Section 3.4), which enhances the ISC efficiency. Due to the increase in the ISC efficiency of the R6-BDP aggregates upon the addition of the shorter alkyl chain IL, their singlet oxygen ($^1O_2$) generation efficiency should be enhanced, which was assessed by a photochemical technique. This study included the addition of C_2C_2im-Br (short alkyl chain IL) to the R6-BDP aggregates and DPBF was added as a singlet oxygen scavenger. The photodegradation of DPBF upon photoirradiation of the BODIPY aggregates was measured by monitoring the decrease in the absorbance of DPBF at 410 nm. It has been observed that the absorption of DPBF is significantly reduced in the presence of singlet oxygen.[65] Firstly, the photodegradation of DPBF was examined in the presence of the R6-BDP aggregates (Fig. 12(b)). The absorption peak intensity of DPBF in the presence of the R6-BDP aggregates showed a slight decrease under laser photoirradiation (Fig. 12(b)). However, its absorption peak intensity at 410 nm decreased rapidly upon addition of C_2C_2im-Br IL on the aggregation of R6-BDP (Fig. 12(c)), indicating that the R6-BDP aggregates generated singlet oxygen more efficiently in the presence of the short alkyl chain IL. The decrease in DPBF concentration over irradiation time was also evident through the drastic color change in the solution, shifting from green to colorless (see inset in Fig. 12(c)). Furthermore, no reaction was observed between the aggregated form +C_2C_2im-Br and DPBF as the absorption band of the photosensitizer at around 525 nm remained unchanged, as shown in Fig. 12(c). The decay rates of DPBF upon the addition of the aggregated form +C_2C_2im-Br are higher than that of the molecular and aggregated forms of R6-BDP (Fig. 12(d)), indicating the efficient photosensitization ability of the singlet oxygen generated by the R6-BDP aggregates in the presence of the short alkyl chain ionic liquid. This result demonstrates the excellent photostability of the aggregated form +C_2C_2im-Br, enabling its use for prolonged laser exposure (high dose) during PDT. Therefore, these results suggest that the impact of C_2C_2im-Br (short alkyl chain IL) on the enhancement of singlet oxygen generation by R6-BDP molecules may play an important role as a photosensitizer in photodynamic therapy.

3.6. *In vitro* photodynamic therapy evaluation in cancer cells

An *in vitro* photodynamic therapeutic investigation was performed using the MTT method both with and without illumination using 490 nm LED light. The cytotoxicity of the R6-BDP aggregates with the addition of the short alkyl chain IL (C_2C_2im-Br) on HeLa cells was assessed at concentrations of 0.2 μM, 2 μM, 4 μM and 8 μM. As shown in Fig. 13, the cytotoxicity was low for aggregates of R6-BDP even at the dose of 8 μM compared to aggregated form +C_2C_2im-Br in the dark as well as under light irradiation. Furthermore, the addition of the short alkyl chain IL to the R6-BDP aggregates incubated at concentrations of 0.2 μM, 2 μM, 4 μM and 8 μM in the dark caused 19%, 23%, 39% and 44% cell death in the HeLa cells, respectively. In contrast, a significant increase in cell death was observed after exposure to light, as shown in Fig. 13. Therefore, R6-BDP aggregation in the presence of C_2C_2im-Br could potentially enhance its role as a photosensitizer for photodynamic therapy.

3.7. Intracellular singlet oxygen ($^1O_2$) detection

To explore the therapeutic mechanism of the effect of ionic liquids on R6-BDP aggregate-mediated PDT, we further verified the generation of singlet oxygen in HeLa cells by fluorescence microscopy imaging using 2,7-dichlorofluorescein diacetate (DCFH-DA) as an reactive oxygen species (ROS) indicator.[46]

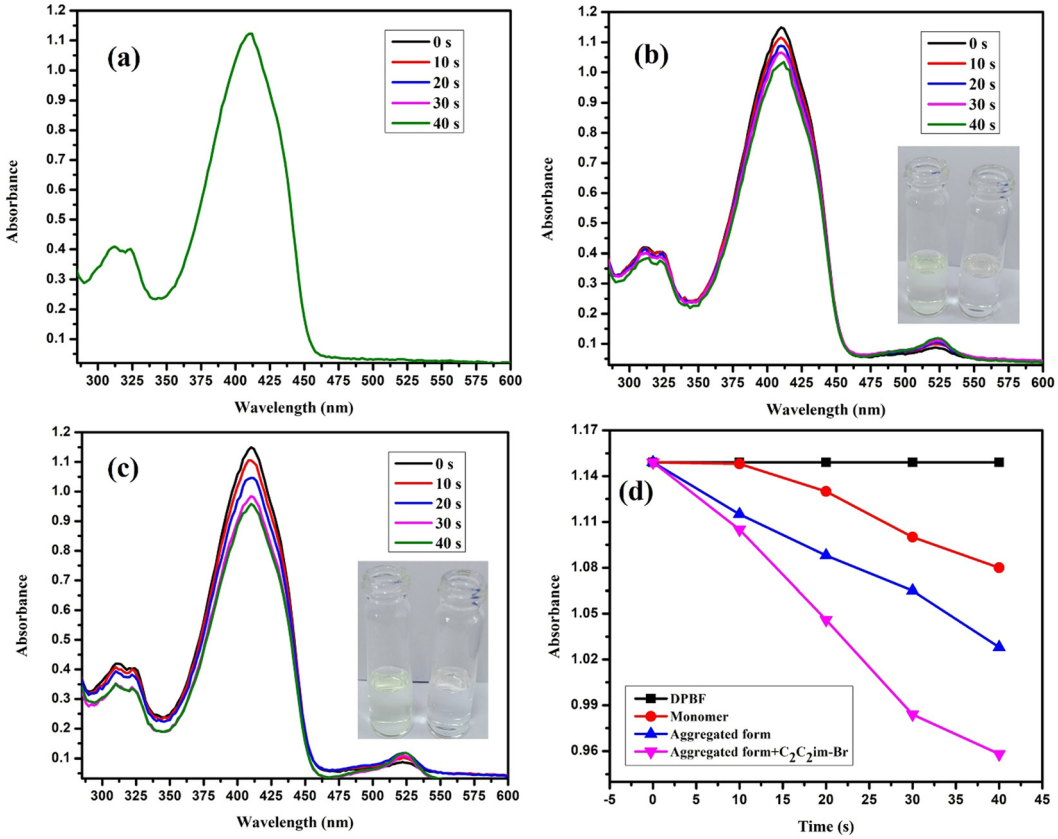

Fig. 12 Absorbance spectra of (a) DPBF with time, (b) DPBF in the presence of R6-BDP aggregates, (c) DPBF in the presence of aggregated form +C_2C_2im-Br and (d) comparison of the decay rates of DPBF, R6-BDP molecular and aggregated forms, and the aggregated form +C_2C_2im-Br at 410 nm, with higher rates indicating more efficient photosensitization capabilities of $^1O_2$.

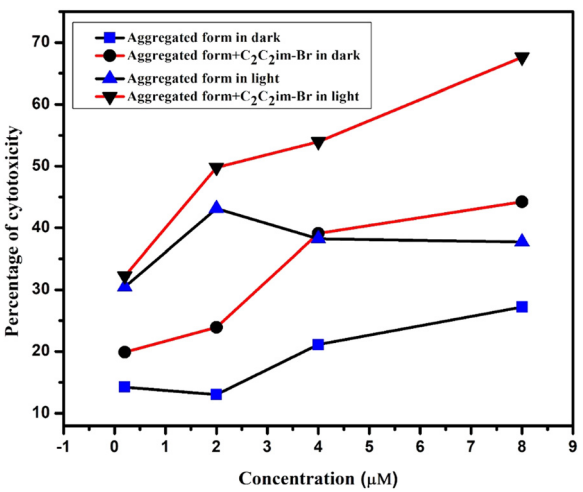

Fig. 13 *In vitro* cytotoxicity of the aggregated form of R6-BDP and aggregated form +C_2C_2im-Br on HeLa cells in the dark and under light illumination.

Intracellular esterase can hydrolyse DCFH-DA to create DCFH, which resists cell membrane penetration and allows ROS within the cell, subsequently oxidizing DCFH to create fluorescent DCF (2,7-dichlorofluoresce) to emit bright green fluorescence.[66] HeLa cells were incubated with the DCFH-DA + aggregated form of R6-BDP and DCFH-DA+ aggregated form of R6-BDP + C_2C_2im-Br in a dose-dependent manner at concentrations of 0.2 μM, 2 μM, 4 μM and 8 μM with and without light irradiation.

As shown in Fig. 14, the HeLa cells exhibited high DCF green fluorescence in the presence of the aggregated form of R6-BDP following 490 nm irradiation, indicating that the cells contained an abundance of $^1O_2$. The green fluorescence was greater at a higher dose (4 μM and 8 μM) under irradiation with light, indicating more singlet oxygen generation at the doses of 4 μM and 8 μM. In contrast, the green fluorescence was less in the dark compared to that in the light. This is an indication of an efficient photosensitizer that is helpful for PDT. After the incubation of HeLa cells with aggregated form +C_2C_2im-Br, the production of singlet oxygen was greater under light, showing more green fluorescence than that in the dark. In addition, more singlet oxygen was generated than that by the R6-BDP aggregates. The generation of more singlet oxygen after the addition of the short alkyl chain ionic liquid (C_2C_2im-Br) to the R6-BDP aggregates indicates the formation of a more solidified form of R6-BDP. This helps in transferring energy to molecular oxygen, producing singlet oxygen due to the low energy gap between the singlet and triplet states. These data

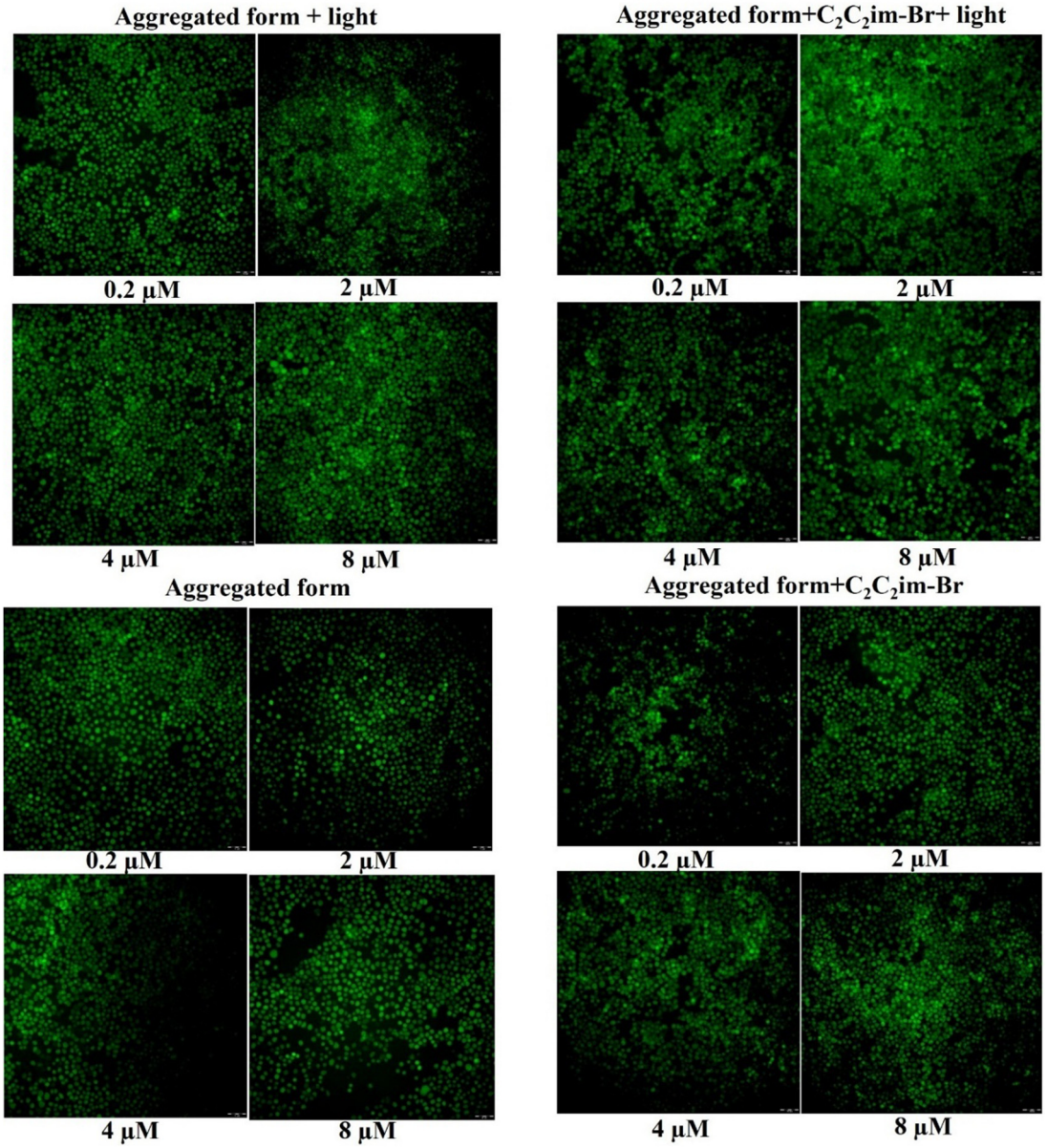

Fig. 14 Confocal fluorescence images of intracellular $^1O_2$ production in HeLa cells using DCFH-DA as an indicator.

clearly indicate that ionic liquids have potential to increase the intracellular generation of singlet oxygen *via* the aggregation of R6-BDP for PDT treatment.

4. Conclusion

In this study, we explored the aggregation behaviour of a BODIPY molecule derivative (R6-BDP) through various spectroscopic, microscopic, and computational techniques. We also examined the influence of the cationic chain length of symmetrical ionic liquids on the aggregation of R6-BDP. Three ionic liquids with varying alkyl chain lengths on the cationic moiety were synthesized to examine how increasing the cationic alkyl chain length affects the aggregation of R6-BDP. Photophysical studies were conducted on both the molecular and aggregated forms of the R6-BDP molecule. The absorption profile of the R6-BDP aggregates exhibited a red shift compared to its molecular form, and the spectral data suggested the formation of J-aggregates. Notably, we observed the formation of ''red-shifted H-aggregates'', which is an uncommon phenomenon in this context. Further investigation revealed that the addition of a shorter alkyl chain IL (C_2C_2im-Br) promoted the stronger aggregation of R6-BDP, decreasing the energy gap between its singlet and triplet excited states. This enhanced aggregation improved the generation of singlet oxygen, which can have important implications for photodynamic therapy in cancer treatment. In contrast, the presence of a longer alkyl chain IL (C_8C_8im-Br) led to dissociation of the aggregates, converting them back to the molecular form. Notably, no significant effect on R6-BDP aggregation was observed with a medium-length

alkyl chain IL (C_4C_4im-Br). These findings highlight the significant role of the cation chain length of ILs in modulating the aggregation state of R6-BDP, with potential applications in PDT and drug delivery. Short alkyl chain ionic liquids appear to favour the formation of more stable organic aggregates, while longer chains disrupt this aggregation. The theoretical DFT and TD-DFT results also supported the experimental findings. Biological studies revealed that the addition of a shorter alkyl chain IL to the R6-BDP aggregates enhanced singlet oxygen generation, improving their photodynamic therapeutic performance. The solidified form of R6-BDP aggregates, resulting from the addition of a short alkyl chain IL, boosted singlet oxygen production and photocytotoxicity. These findings demonstrate the potential of ionic liquids in optimizing R6-BDP aggregates for effective PDT treatment. Further research is required to expand our understanding of these effects and explore their therapeutic potential.

Conflicts of interest

There are no conflicts to declare.

Data availability

^{1}H NMR spectrum of R6-BDP, $^{13}C\{^1H\}$ NMR spectrum of R6-BDP, ^{1}H NMR spectrum of C_2C_2im-Br, HR-MS analysis of C_2C_2im-Br, ^{1}H NMR spectrum of C_4C_4im-Br, HR-MS analysis of C_4C_4im-Br, ^{1}H NMR spectrum of C_8C_8im-Br, HR-MS analysis of C_8C_8im-Br, absorption spectra of R6-BDP in molecular and aggregated forms, ultraviolet-visible absorption and fluorescence spectra of aggregated state of R6-BDP with gradual addition C_4C_4im-Br, fluorescence intensity of R6-BDP aggregates vs concentration of IL (C_8C_8im-Br), DLS-based particle size data analysis of R6-BDP aggregates, aggregation + C_2C_2im-Br, aggregation + C_4C_4im-Br, aggregation + C_8C_8im-Br, and tri-exponential fitting parameters and average lifetimes for the aggregated form and aggregated form in the presence of C_2C_2im-Br, C_4C_4im-Br and C_8C_8im-Br. Excitation energies (eV) of the S_1, S_2, S_3, T_1, T_2, and T_3 states of monomer and dimers of R6-BDP. See DOI: **https://doi.org/10.1039/d5cp01890k**

The data supporting this article have been included as part of the SI.

Acknowledgements

This work was supported by the Department of Science and Technology (DST), Government of India, New Delhi (award no. DST/INSPIRE/04/2022/002706). N. N. Das and Dr D. Majhi express their gratitude to the DST INSPIRE Faculty Program for the fellowship/research grant and financial support. Dr D. Majhi also thank the National Institute of Technology, Tiruchirappalli (NITT), for providing the necessary infrastructure facilities and the 'Central Facility for Time-Resolved Spectroscopy and Microscopy' at IIT Bombay for the time-resolved fluorescence decay measurements.

References

1 J. Bañuelos, *Chem. Rec.*, 2016, **16**, 335–348.
2 S. Mula, *BODIPY: A Unique Dye for Versatile Optical Applications*, Springer Nature, 2024, vol. 1, pp. 369–399.
3 A. Loudet and K. Burgess, *Chem. Rev.*, 2007, **107**, 4891–4932.
4 M. Gupta, S. Mula, M. Tyagi, T. K. Ghanty, S. Murudkar, A. K. Ray and S. Chattopadhyay, *Chem. – Eur. J.*, 2013, **19**, 17766–17772.
5 M. Liu, S. Ma, M. She, J. Chen, Z. Wang, P. Liu, S. Zhang and J. Li, *Chin. Chem. Lett.*, 2019, **30**, 1815–1824.
6 H. Lu, J. Mack, Y. Yang and Z. Shen, *Chem. Soc. Rev.*, 2014, **43**, 4778–4823.
7 G. Ulrich, R. Ziessel and A. Harriman, *Angew. Chem. Int. Ed.*, 2008, **47**, 1184–1201.
8 S. Mula and M. Koli, *Chem. Med. Chem.*, 2024, **19**, e202400041.
9 I. S. Yadav and R. Misra, *J. Mater. Chem. C*, 2023, **11**, 8688–8723.
10 M. K. Choudhary and S. Mula, *New J. Chem.*, 2023, **47**, 9045–9049.
11 Y. Dong, P. Kumar, P. Maity, I. Kurganskii, S. Li, A. Elmali, J. Zhao, D. Escudero, H. Wu, A. Karatay, O. F. Mohammed and M. Fedin, *Phys. Chem. Chem. Phys.*, 2021, **23**, 8641–8652.
12 J. Zhao, K. Chen, Y. Hou, Y. Che, L. Liu and D. Jia, *Org. Biomol. Chem.*, 2018, **16**, 3692–3701.
13 M. Koli, S. Gupta, S. Chakraborty, A. Ghosh, R. Ghosh, A. P. Wadawale, T. K. Ghanty, B. S. Patro and S. Mula, *Chem. – Eur. J.*, 2023, **29**, e202301605.
14 X. Zhang, Z. Wang, Y. Hou, Y. Yan, J. Zhao and B. Dick, *J. Mater. Chem. C*, 2021, **9**, 11944–11973.
15 D. Simionesie, G. O'Callaghan, J. R. H. Manning, T. Düren, J. A. Preece, R. Evans and Z. J. Zhang, *Polycyclic Aromat. Compd.*, 2023, **43**, 3790–3809.
16 Y. S. Marfin, E. A. Banakova, D. A. Merkushev, S. D. Usoltsev and A. V. Churakov, *J. Fluoresc.*, 2020, **30**, 1611–1621.
17 Y. F. Kang, W. K. Chen, K. X. Teng, L. Y. Wang, X. C. Xu, L. Y. Niu, G. Cui and Q. Z. Yang, *CCS Chem.*, 2022, **4**, 3516–3528.
18 D. Simionesie, G. O'Callaghan, J. R. H. Manning, T. Düren, J. A. Preece, R. Evans and Z. J. Zhang, *Polycyclic Aromat. Compd.*, 2023, **43**, 3790–3809.
19 Y. S. Marfin, E. A. Banakova, D. A. Merkushev, S. D. Usoltsev and A. V. Churakov, *J. Fluoresc.*, 2020, **30**, 1611–1621.
20 K. Kataoka, G. S. Kwon, M. Yokoyama, T. Okano and Y. Sakurai, *J. Controlled Release*, 1993, **24**, 19–132.
21 K. Kataoka, A. Harada and Y. Nagasaki, *Adv. Drug Delivery Rev.*, 2012, **64**, 37–48.
22 J. Chen, S. Li, Z. Wang, Y. Pan, J. Wei, S. Lu, Q. W. Zhang, L. H. Wang and R. Wang, *Chem. Sci.*, 2021, **12**, 7727–7734.
23 N. Rapoport, *Prog. Polym. Sci.*, 2007, **32**, 962–990.
24 S. Ghosh, C. Ghatak, C. Banerjee, S. Mandal, J. Kuchlyan and N. Sarkar, *Langmuir*, 2013, **29**, 10066–10076.
25 S. Mandal, J. Kuchlyan, S. Ghosh, C. Banerjee, N. Kundu, D. Banik and N. Sarkar, *J. Phys. Chem. B*, 2014, **118**, 5913–5923.

26 S. S. Dandpat and M. Sarkar, *Phys. Chem. Chem. Phys.*, 2015, **17**, 13992–14002.
27 L. G. Celia-Silva, R. N. Martins, A. J. P. Carvalho, J. P. P. Ramalho, P. Morgado, E. J. M. Filipe and L. F. G. Martins, *Energy Fuels*, 2022, **36**, 9048–9065.
28 R. N. Martins, L. G. Celia-Silva, J. P. P. Ramalho, P. Morgado, E. J. M. Filipe and L. F. G. Martins, *Energy Fuels*, 2024, **38**, 3693–3712.
29 S. Rani, D. Bagchi, U. Pal, M. Kumari, M. Sharma, A. Bera, J. Shabir, S. K. Pal, T. Saha-Dasgupta and S. Mozumdar, *ACS Omega*, 2020, **5**, 25582–25592.
30 C. Ghatak, V. G. Rao, S. Mandal, S. Ghosh and N. Sarkar, *J. Phys. Chem. B*, 2012, **116**, 3369–3379.
31 D. Majhi, A. V. Komolkin and S. V. Dvinskikh, *Int. J. Mol. Sci.*, 2020, **21**, 1–14.
32 S. P. Verevkin, D. H. Zaitsau, R. N. Nagrimanov, Y. Zhang, E. J. Maginn and A. Stark, *J. Mol. Liq.*, 2024, **395**, 123850.
33 W. Zheng, A. Mohammed, L. G. Hines, D. Xiao, O. J. Martinez, R. A. Bartsch, S. L. Simon, O. Russina, A. Triolo and E. L. Quitevis, *J. Phys. Chem. B*, 2011, **115**, 6572–6584.
34 D. Majhi, A. Pabbathi and M. Sarkar, *J. Phys. Chem. B*, 2016, **120**, 193–205.
35 E. Binetti, A. Panniello, L. Triggiani, R. Tommasi, A. Agostiano, M. L. Curii and M. Striccoli, *J. Phys. Chem. B*, 2012, **116**, 3512–3518.
36 D. Majhi and M. Sarkar, *Phys. Chem. Chem. Phys.*, 2017, **19**, 23194–23203.
37 A. Ghosh, C. K. De, T. Chatterjee and P. K. Mandal, *Phys. Chem. Chem. Phys.*, 2015, **17**, 16587–16593.
38 S. Gorai, R. Agrawal, R. Ghosh and S. Mula, *Chem. – Eur. J.*, 2024, **30**, e202402669.
39 A. Dimitrijević, N. Zec, N. Zdolšek, S. Dožić, A. Tot, S. Gadžurić, M. Vraneš and T. Trtić-Petrović, *J. Ind. Eng. Chem.*, 2016, **40**, 152–160.
40 D. Majhi, S. K. Das, P. K. Sahu, Md. S. Pratik, A. Kumar and M. Sarkar, *Phys. Chem. Chem. Phys.*, 2014, **16**, 18349–18359.
41 M. Z. K. Baig, D. Majhi, R. N. P. Tulichala, M. Sarkar and M. Chakravarty, *J. Mater. Chem. C*, 2017, **5**, 2380–2387.
42 Y. Kim, T. Jun, S. V. Mulay, S. T. Manjare, J. Kwak, Y. Lee and D. G. Churchill, *Dalton Trans.*, 2017, **46**, 4111–4117.
43 N. Gupta, S. I. Reja, V. Bhalla, M. Gupta, G. Kaurb and M. Kumar, *J. Mater. Chem. B*, 2016, **4**, 1968–1977.
44 A. H. Pandith, N. Islam, Z. F. Syed, S. Rehman, S. Bandaru and A. Anoop, *Chem. Phys. Lett.*, 2011, **516**, 199–203.
45 T. Mosmann, *J. lmmunol. Methods*, 1983, **65**, 55–63.
46 R. Cathcart, E. Schwiers and N. B. Ames, *Anal. Biochem.*, 1983, **134**, 111–116.
47 M. Kasha, H. R. Rawls and M. A. Bayoumi, *Pure Appl. Chem.*, 1965, **11**, 371–392.
48 N. J. Hestand and F. C. Spano, *Chem. Rev.*, 2018, **118**, 7069–7163.
49 F. C. Spano, *Acc. Chem. Res.*, 2010, **43**, 429–439.
50 C. Zheng, C. Zhong, C. J. Collison and F. C. Spano, *J. Phys. Chem. C*, 2019, **123**, 3203–3215.
51 Z. Liu, Z. Jiang, M. Yan and X. Wang, *Front. Chem.*, 2019, **7**, 1–16.
52 S. Ghosh, B. Jana, A. Ghosh, D. M. Guldi and A. Patra, *J. Phys. Chem. Lett.*, 2021, **12**, 3424–3430.
53 R. Dutta, S. Kundu and N. Sarkar, *Biophys. Rev.*, 2018, **10**, 861–871.
54 C. K. De, A. Ghosh and P. K. Mandal, *J. Phys. Chem. B*, 2022, **126**, 1551–1557.
55 M. N. Vaghela, V. N. Sastry and K. V. Aswal, *Colloid Polym. Sci.*, 2011, **289**, 309–322.
56 S. Christau, T. Moeller, J. Genzer and R. Koehler, *Macromolecules*, 2017, **50**, 7333–7343.
57 M. Blesic, M. H. Marques, N. V. Plechkova, K. R. Seddon, L. P. N. Rebelo and A. Lopes, *Green Chem.*, 2007, **9**, 481–490.
58 M. H. Gehlen, *J. Photochem. Photobiol. C Photochem. Rev.*, 2020, **42**, 100338.
59 M. C. Marian, *Annu. Rev. Phys. Chem.*, 2021, **72**, 617–640.
60 J. T. Penfold, E. Gindensperger, C. Daniel and C. M. Marian, *Chem. Rev.*, 2018, **118**, 6975–7025.
61 L. Estergreen, A. R. Mencke, D. E. Cotton, N. V. Korovina, J. Michl, S. T. Roberts, M. E. Thompson and S. E. Bradforth, *Acc. Chem. Res.*, 2022, **55**, 1561–1572.
62 F. Sabuzi, M. Stefanelli, D. Monti, V. Conte and P. Galloni, *Molecules*, 2020, **25**, 133.
63 Q. Wan, J. Xia, W. Lu, J. Yang and C. M. Che, *J. Am. Chem. Soc.*, 2019, **141**, 11572–11582.
64 K. Magesh, L. Y. Hsun, S. P. Wu and S. Velmathi, *Appl. Bio Mater.*, 2024, **7**, 5679–5688.
65 Y. C. Lai, S. Y. Su and C. C. Chang, *ACS Appl. Mater. Interfaces*, 2013, **5**, 12935–12943.
66 N. M. Idris, M. K. Gnanasammandhan, J. Zhang, P. C. Ho, R. Mahendran and Y. Zhang, *Nat. Med.*, 2012, **18**, 1580–1585.

